

PVP-derived TiO₂/C and TiO₂/C/N Nanofibers by SBS with High Adsorption/Photocatalytic Capacity

Rosiane M. C. Farias^{a*}, Samuel B. Araújo^b, Herbet B. Sales^a, Raquel S. Leite^a

Rondinele N. Araujo^a, Emanuel P. Nascimento^a, Gelmires A. Neves^a, Romualdo R. Menezes^a

^aUniversidade Federal de Campina Grande, Departamento de Engenharia de Materiais, Laboratório de Tecnologia de Materiais, Campina Grande, PB, Brasil.

^bUniversidade Federal de Campina Grande, Programa de Pós-Graduação em Ciência e Engenharia de Materiais, Campina Grande, PB, Brasil.

Received: November 27, 2023; Revised: February 04, 2024; Accepted: February 14, 2024

A solution blow spinning (SBS) process was utilized to create nanofibers of TiO₂/C and TiO₂/C/N with potential applications in photocatalysis and dye adsorption. Polyvinylpyrrolidone was used as a carbon and nitrogen source. Their content in the TiO₂ structure decreased as the temperature increased from 350 to 550 °C. Physical-chemical, morphological, and structural features were investigated. Adsorption and photodegradation experiments revealed that the material calcined at 400 °C had higher dye removal (98%) under dark settings, whereas the greater photodegradation efficiency under visible and UV light was 56% and 98%, respectively, for the sample calcined at 550 °C. The results suggest that the SBS has the potential to develop an efficient adsorbent and photocatalyst for use in treatments of contaminated water.

Keywords: Polyvinylpyrrolidone, TiO₂/C, TiO₂/C/N, nanofibers, solution blow spinning, adsorption, photocatalysis.

1. Introduction

In recent years, wastewater remediation has emerged as one of the most innovative environmental applications. This is crucial for safeguarding the environment, promoting public health and the sustainable use of water resources, and contributing to a healthier, more balanced future¹. Photocatalysis and adsorption stand out among the methods used for this objective. In a photocatalytic process, adsorption and reaction occur simultaneously, converting pollutant molecules into harmless products²⁻⁴. They can effectively remove dyes and other organic contaminants from aqueous solutions^{5,6}.

Titanium dioxide (TiO₂) is the most employed semiconductor in photocatalysis. Due to its unique properties, chemical stability, and low cost⁷, is a versatile and extremely effective photocatalyst. TiO₂ can generate electron-hole pairs when exposed to light energy, which can participate in a variety of photochemical reactions. These reactions may entail the decomposition of organic pollutants, the production of reactive oxygen species, or the reduction of molecules⁸. However, TiO₂ has a wide bandgap (3.2 eV), consequently, its photocatalytic activity is particularly effective in the ultraviolet (UV) region of the electromagnetic spectrum, in addition to exhibiting rapid electron/hole recombination^{7,9}. Because of this, several researchers have investigated and developed TiO₂ in combination with other substances forming various binary and ternary compounds to extend the light absorption range in the visible light spectrum^{10,11}. TiO₂/carbon (TiO₂/C) and TiO₂/carbon/nitrogen (TiO₂/C/N) nanocomposite has been extensively studied due to its potential for advanced applications such

as dye-sensitized solar cells¹², anode material for sodium-ion batteries¹³⁻¹⁵, an electrode for supercapacitors^{16,17}, electrochemical sensor¹⁸, electrocatalysis and photocatalysis¹⁹⁻²⁵. When TiO₂ is combined with carbon, it can manifest several improved properties compared to pure TiO₂²⁶.

Carbon acts as a sensitizer by narrowing the bandgap of TiO₂, allowing the composite material to capture a broader range of light energy, including visible light²⁷⁻³⁰. This is an essential strategy, as it becomes possible to utilize a larger portion of solar radiation, which is more abundant and accessible compared to UV light^{31,32}. TiO₂ photo-excited generates pair electron holes that can be accepted by the carbon, resulting in an efficient charge separation³³. In addition, carbon and N-carbon-based materials can be excellent adsorbents for dyes and other organic compounds³⁴. These materials have a high surface area, porosity, and chemical reactivity, which also make them effective for adsorption processes³⁵⁻³⁷.

Most nanocomposites consist of TiO₂ nanoparticles embedded^{15,38} or decorated into carbon nanofibers^{13,39,40}. This heterostructure can reduce the active sites of the particles by the probability of self-agglomeration. However, 1D nanofibers have attracted special interest in recent years because this morphology increases the specific surface area and improves the contact with molecules and ions of interest. Studies^{41,42} developed 1D TiO₂/C composites using electrospinning, but no study used solution blow spinning (SBS) to produce TiO₂/C composites, despite the advantages of SBS⁴³. In the last five years, SBS has shown remarkable performance in the production of nanofibers as the process is readily scalable for large-scale production, and a wide variety of polymers, solvents, and ceramics precursors can be employed⁴⁴⁻⁴⁹.

*e-mail: ziane.costa@gmail.com

Moreover, studies⁵⁰⁻⁵⁴ depicted the feasibility and success of SBS in the production of ceramic nanofibers using non-toxic or low-toxic solvents, such as water and ethanol improving its capability to produce nanofibrous structures.

Polyvinylpyrrolidone (PVP) is widely used as a precursor polymer in ceramic spinning due to its solubility in environmentally friendly solvents (such as water and ethanol), spinnability, and ability to produce stable nanofibers^{55,56}. Typically, PVP functions as a sacrificial polymer during spinning, providing a temporary support structure. PVP is also considered a source of carbon and nitrogen^{37,57}, however, its use for this purpose is still scarce. In addition, there were no reports of PVP-based TiO₂/C and TiO₂/C/N nanofibers produced by the SBS technique. Thus, in this study, we reported for the first time the synthesis of TiO₂-PVP nanofibers to obtain TiO₂/C and TiO₂/C/N nanofibers by SBS followed by a calcination process at temperatures varying from 350 °C to 550 °C, where PVP have the function of viscosity aid but also, and the most, to be used as precursor of C and N, what make possible the use of more green solvent. The influence of temperature calcination on the composition, physical-chemical, morphological, and structural properties of provided nanofibers was evaluated. The photocatalytic (under UV and visible light) and adsorptive performances were also evaluated using crystal violet (CV) dye as a contaminant model.

2. Experimental

Titanium(IV) isopropoxide (TTIP - Aldrich, 99%) was used as the precursor of TiO₂ content. Acetic Acid (Química Moderna) and ethanol (Cinética, 99.5%) as the solvent. Polyvinylpyrrolidone, PVP (Aldrich, average Mw ~1,300,000) was used as an assistant spinning solution and as a carbon source. The cationic dye, crystal violet (CV) (P.A., Synth, Mw 408.0 g mol⁻¹), was used in the adsorption experiments.

An SBS apparatus was used to produce the TiO₂-PVP nanofibers. It consists of a syringe pump, a concentric nozzle array, a pressurized air source, a pressure regulator, a heat source, and a collector. The SBS was set up based on the methodology described previously to produce nanofibers^{37,52}. Briefly, PVP (0.8 g) was dissolved in ethanol, while TTIP was dissolved in a mixture of ethanol/acetic acid. The solutions were combined and agitated for 60 minutes. The final solution consisted of 8% PVP (w/v), resulting in a viscous mixture that was used for SBS. Pressured air and the injection rate solution were adjusted to 6.9 kPa and 6.6 ml h⁻¹, respectively. Fiber formation was carried out at a temperature of approximately 60 °C and the working distance (tip to collector distance) was set at 450 mm. After spinning, the fibers with a cotton-wool-like structure were placed in a laboratory oven for five days. Then, the fibers were calcinated in air condition at 350, 400, 450, 500, and 550 °C for 1 h with a heating rate of 10 °C min⁻¹. The samples were denoted based on the temperature calcination Ti-350°C, Ti-400°C, Ti-450°C, Ti-500°C and Ti-550°C.

2.1. Characterization

The thermogravimetric (TG) and differential thermal (DTA) analysis of the nanofibers was carried out simultaneously (SHIMADZU, DTG-60H under an atmosphere of synthetic

air, and a constant heating rate of 5 °C/min. Sample morphology was conducted using a scanning electron microscope (TESCAN, VEGA4). ImageJ software evaluated diameter size (version 1.48, National Institutes of Health, Bethesda, MD, USA). Tuket test statistical analysis was performed at a 0.05 level of significance. Fourier transform infrared spectroscopy (FTIR) (IR Prestige-21 Affinity-1 FTIR 8400S) was recorded in the spectral range from 4000 to 400 cm⁻¹, with 32 scanning and 4 cm resolutions. A LECO elemental analyzer, CHN268, with EDTA standard, operating at 950 °C was used to estimate the amount of carbon, hydrogen, and nitrogen. X-ray diffraction (Shimadzu, XRD 6000) with Cu K α radiation ($\lambda = 0.154$ nm) was obtained with a scanning speed of 5°/min. Raman spectrum (RENISHAW, MS30 ENCODED STAGE) was used to investigate the crystallinity of nanofibers using a laser of 532 nm. UV-Vis spectroscopy (Shimadzu, UV-2600i) was used to obtain the diffuse reflectance spectroscopy (DRS) spectra in the UV-Vis region to estimate the band gap. The Kubelka-Munk function was used by the Tauc plot to determine the band gap. Brunauer-Emmett-Teller (BET) surface area model was calculated from data from the Nitrogen adsorption/desorption experiment for nanofibers performed at 77 K (Autosorb iQ-C, NOVA 3200 model); Barrett-Joyner-Halenda (BJH) model was used to calculate the pore volume and the pore size.

2.2. Adsorption and degradation tests

Adsorption and degradation experiments were carried out for dye removal of 10 mg L⁻¹ CV aqueous solution (pH 7) with a shaker incubator (NT 735, Nova Técnica, Brazil) operated at 25 °C at a speed of 100 rpm. The dosage of the nanofibers was fixed at 5 mg and the volume of the CV solution was 10 ml for both adsorption and photocatalytic tests. The concentrations of the CV solutions were analyzed by UV-vis spectroscopy (Shimadzu, UV-1800) in the range of 400 to 800 nm. The adsorption reaction was carried out in the absence of light. To achieve adsorption equilibrium, the nanofibers/CV solutions were stirred at 100 rpm in the dark for 360 minutes. The concentrations of the solutions were evaluated over time. After 180 minutes the adsorption/desorption reached equilibrium, then, solutions/fibers were exposed for 240 minutes to visible light using 4 incandescent lamps (total irradiation power of 160 W) and to ultraviolet light using a blue UV lamp (9 W). The distance between the lamps and the solution was fixed at 15 cm. Every 30 minutes, aliquots of the solutions were collected, and centrifuged and their concentrations were analyzed by UV-vis spectroscopy (Shimadzu, UV-1800). Photolysis tests for the dye solution were performed under UV and visible light without catalyst/adsorbent. All tests were carried out in triplicates. To calculate the removal percentage, the CV concentration was measured by UV-vis spectrophotometer at λ_{\max} 580 nm for samples calcined at 350 °C and 400 °C. For samples calcined at 450, 500, and 550 °C, λ_{\max} 555 nm was used due to the hypsochromic shift. Equation 1 was used to calculate the percentage removal, where C_0 and C_f are the initial and final dye concentrations, respectively.

$$\% \text{ Removal / Degradation} = \left(C_0 - C_f / C_0 \right) 100 \quad (1)$$

The kinetic study was based on the experimental degradation data of CV under UV and Visible lights for the samples calcined at 450, 500, and 550 °C. The rate constant (K) for reaction degradation was calculated using Equation 2, where C_t is the concentration at a specific irradiation time and K is the reaction rate constant, which represents the slope of the curve plotted as $-\ln(C_t/C_0)$ versus t (time).

$$-\ln\left(\frac{C_t}{C_0}\right) = Kt \quad (2)$$

3. Results

The thermogravimetric analysis (TG/DTG) and differential thermal analysis (DTA) curves of the as-spun PVP-TiO₂ nanofibers are shown in Figure 1a, b. The first stage of mass loss occurred between room temperature and 117 °C with approximately 13.2% loss, associated with the evaporation of residual ethanol and/or moisture. The mass of the sample gradually reduced while the temperature increased until around 230 °C, when the second mass loss event began, marked by a more intense reduction, about 36.7% up to 377 °C. It refers to the beginning of the degradation of the PVP polymer, related to the degradation of its side chain. The third loss stage occurs up to approximately 500 °C with about 23% loss and can be attributed to the removal of the PVP chains closest to the TiO₂ surface and subsequent evaporation of the volatile by-products of polymer decomposition³⁷. In the end, there was a further gradual loss of mass up to 700 °C, resulting in a residual mass of 25.6%.

The DTA thermogram (Figure 2b) shows an endothermic peak up to 100 °C with a maximum of 47 °C, resulting from the evaporation of free water and water molecules physically adsorbed on the TiO₂ surface by hydrogen bonds. The exothermic peak at 330 °C refers to the thermal degradation of PVP and the elimination of by-products of this process. The exothermic peak at 436 °C is indicative of the beginning of a structural reorganization, through the phase transformation from anatase to rutile TiO₂. These results are consistent with other authors that employ PVP-TiO₂ to generate TiO₂ nanofibers by electrospinning^{58,59}.

Figure 2a-e shows SEM images and the diameter distribution graphics of fibrous systems calcined from 350 °C to 550 °C. All samples present fibers elongated and randomly oriented. The lowest mean diameter value is that of the sample Ti-550 °C (264 ± 132 nm). This result was expected due to the greater shrinkage of the fiber due to the higher calcination temperature and lower amount of carbon residues in the titania structure. The average diameter of the other samples ranged from 305 ± 155 nm to 352 ± 150 nm. These results are in agreement with TiO₂ nanofibers spun by SBS reported in the literature, with smaller or similar diameters. For example, Costa et al.⁵¹ and Santos et al.⁵² obtained TiO₂ nanofibers by SBS with average diameters ranging from 334 nm to 594 nm and 206 ± 85 nm to 270 ± 55 nm, respectively. They used different polymers as spinning aids, including PVP. Furthermore, the difference between the average fiber diameter after each calcination temperature is only statistically significant when the comparison is between the highest temperature and the other temperatures, as confirmed by the Tukey test at a level of 0.05 (Figure 2f). On the other hand, the mean diameter of the other fibers did not present statistical significance difference. This indicates that, for most samples, the results showed that neither spinning process factors (such as PVP concentration, injection rate, air pressure, and temperature of the spinning environment) nor calcination temperatures affected the diameter and the formation of nanofibers.

Figure 3 illustrates the FTIR spectra of the Ti-(350-550°C) nanofibers. In all samples, a characteristic broad band of the OH group can be identified in the region of axial stretching around 3420 cm⁻¹. This vibration can be attributed to the presence of physisorbed water and/or residual ethanol. The discrete peak observed at 2237 cm⁻¹ for Ti nanofibers calcined at lower temperatures (350 and 400 °C) is assigned to the stretching of the C≡N. Nitrogen residue is common after partial thermal degradation of PVP. This result can improve the adsorption capacity of the material³⁷. Peaks corresponding to the C-H stretching of the methyl group (CH₃) and the methylene group (CH₂) were observed in 2857 cm⁻¹ and 2927 cm⁻¹, respectively⁶⁰. Despite these peaks being evident only in the Ti-550 °C nanofiber, all samples showed a peak referring to the asymmetric stretching of the C-H vibration in both CH₂ and CH₃ groups at 1394 cm⁻¹.

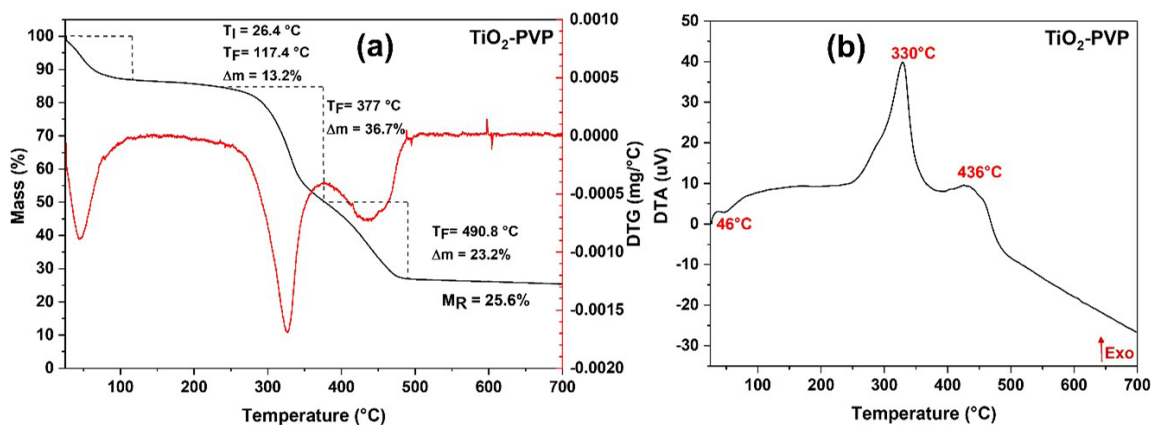


Figure 1. (a) TGA and (b) DTA curves of the PVP-TiO₂ nanofibers.

Ti-O, Ti-O-Ti, and Ti-O-C stretching modes vibrations were identified on the broad band between 400 – 800 cm^{-1} ¹³⁸. The Ti-O-C bonds reflect the connection between the components, which might influence photocatalytic performance by facilitating photoinduced electron transport and minimizing charge carrier recombination⁶¹. The weak band at 1601 cm^{-1} stretching vibration of C=C slightly shifts to 1645 cm^{-1} as calcination temperature increases from 350 to 550 $^{\circ}\text{C}$ ⁶²,

suggesting carbon graphitization due to PVP degradation. According to the elemental analysis, the amount of carbon decreased with increasing calcination temperature from 350 to 450 $^{\circ}\text{C}$. However, between 450 and 550 $^{\circ}\text{C}$, only a slight variation in carbon content was observed (Figure 3b). The results also confirmed the coexistence of C and N, mainly in fibers calcined at a lower temperature, corroborating the vibration peak of the C≡N stretching in the FTIR.

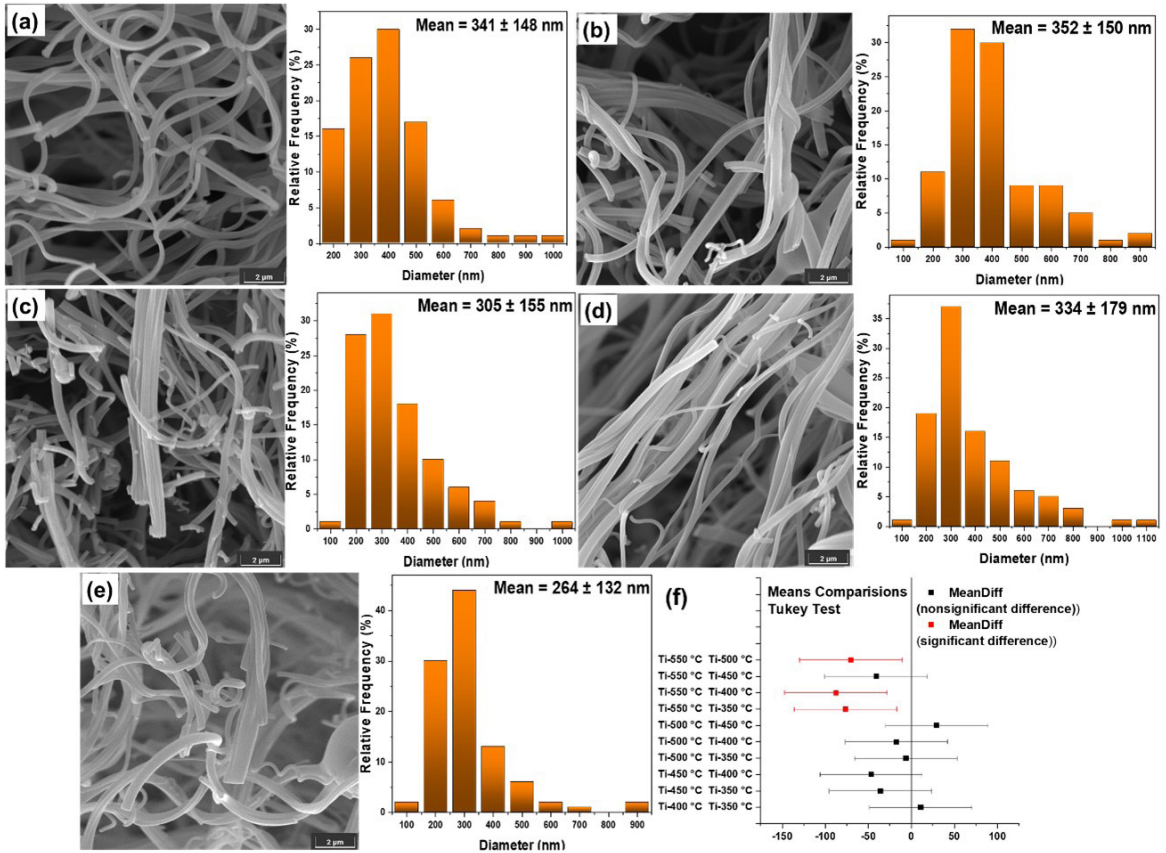


Figure 2. SEM images of and diameter distribution graphics of Ti nanofibers: (a) 350 $^{\circ}\text{C}$, (b) 400 $^{\circ}\text{C}$, (c) 450 $^{\circ}\text{C}$, (d) 500 $^{\circ}\text{C}$, (e) 550 $^{\circ}\text{C}$ and (f) Statistic Tukey Test.

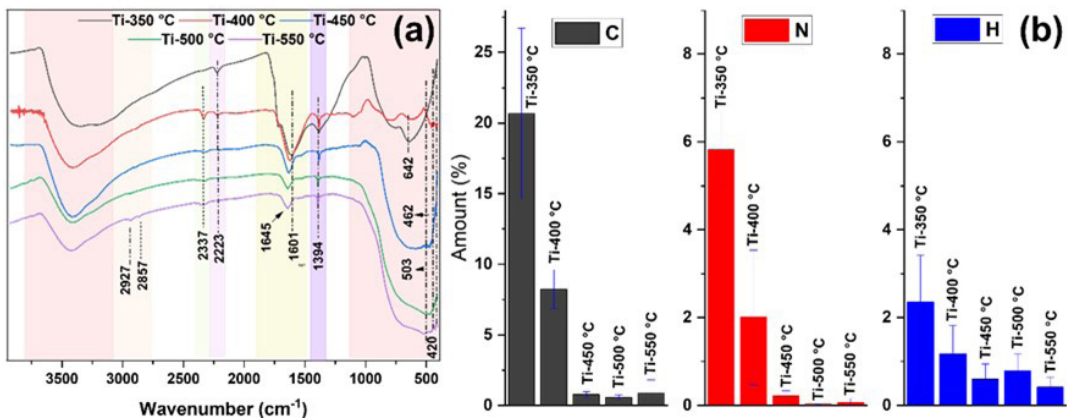


Figure 3. FTIR spectra (a) and elemental analysis (b) of Ti nanofibers prepared at different temperatures.

In this regard, the generation of TiO₂/C and TiO₂/C/N was temperature-dependent under the heat treatment conditions used. Furthermore, the results confirmed the efficiency of using PVP as a source of carbon and nitrogen.

The sample calcined at 350 °C exhibited an XRD pattern (Figure 4) of an amorphous material, with only one wide band with 2θ varying between 15° and 35°, indicating an amorphous structure. On the other hand, samples calcined at a temperature from 400 °C onwards exhibited well-defined peaks on diffractograms. The anatase was the major phase, which is desirable in photocatalytic degradation processes since it proves to be the most photoactive phase. Peaks of the anatase phase (JCPDS card no. 21-1272) at 25.4°, 36.1°, 38°, 48.1°, 54.0°, 55.0° and 62.9° corresponding to the planes (101), (103), (004), (200), (105), (211) were observed. The appearance of peaks referring to the rutile phase becomes more evident in the sample calcined at 500 °C with peaks 2θ at 27.6° (110) and 2θ = 56.5° (002) (JCPDS card N° 086-0148)²⁸. The peaks increase in intensity according to the increase in the calcination temperature. A similar effect was observed on the crystallite size (XS) and the crystallinity (Xc) results. The XS increased from 6.4 to 11.9 nm and the Xc increased from 48.6 to 84.8% (Figure 4b), when the calcination temperature increased from 400 to 550 °C.

Raman spectra of all TiO₂/C calcined nanofibers are exhibited in Figure 4c, d. The samples calcined at 350 °C and 400 °C

exhibited the D band (1365 cm⁻¹) and the G band (1585 cm⁻¹) characteristic of carbon materials, corroborating with other researchers^{1,33,39}. This means that the PVP was degraded into disordered and graphitic carbon at a lower temperature¹⁴. The degree of defects in these carbon samples was evaluated by the ratio of the relative intensity of the D and G bands (I_D/I_G)¹³. The results were 0.95 and 1.02 for TiO₂/C 350 °C and TiO₂/C 400 °C, respectively. It indicates that the degree of defects increased with the increase in calcination temperature. The spectra also show characteristic peaks of vibration modes of anatase TiO₂. The peaks at 147 cm⁻¹, 197 cm⁻¹, and 638 cm⁻¹ are attributed to the E_{1g} (symmetric stretching vibration of O-Ti-O), while the peaks at 400 cm⁻¹ and 519 cm⁻¹ are attributed to B_{1g} (anti-symmetric bending vibration of O-Ti-O). The peak at 519 cm⁻¹ also is assigned to A_{1g} (symmetric bending vibration of O-Ti-O)^{62,63}. As expected, the intensity of these peaks increased as the calcination temperature rose and no evidence of bands referring to carbon was observed at calcination temperatures above 400 °C.

Figure 5a exhibits the N₂ adsorption-desorption isotherms of the Ti nanofibers. According to IUPAC⁶⁴, the isotherms of all samples were classified as type IV characteristics of mesoporous material (range of 2 - 50 nm). The Ti-350 °C and Ti-400 °C isotherms presented the typical H4 hysteresis loop, while the other samples showed type H3. These results reveal slit-shaped pores in samples with type H3 hysteresis and in samples with type H4 hysteresis the pores have narrower slits.

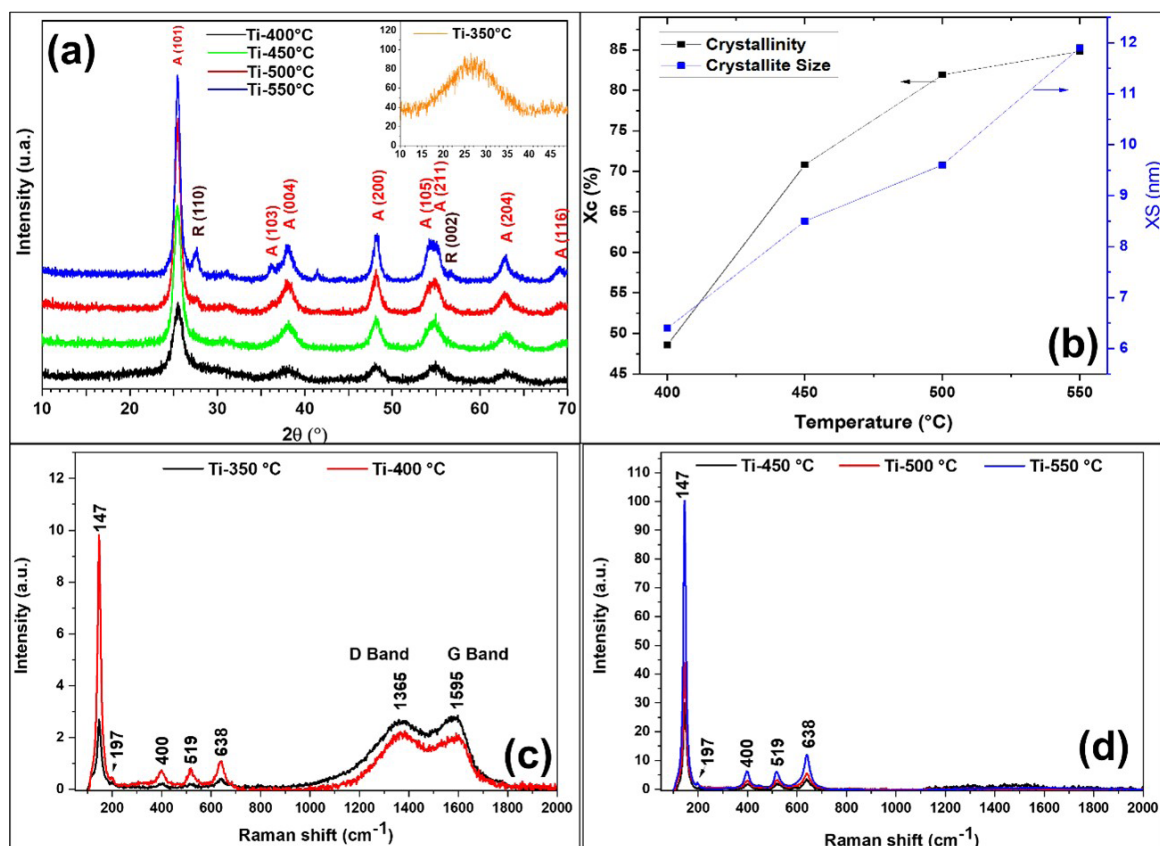


Figure 4. X-ray diffractograms (a) crystallinity and crystallite size (b) and Raman shift (c) and (d) of the nanofibers Ti prepared at different temperatures.

The pores size distributions and the pore data based on the BJH model are displayed in Figure 5b and Table 1, respectively. BET surface areas of the nanofibers are also summarized in Table 1. When the calcination temperature increased from 350 to 400 °C, the surface area and the BJH pore volume increased from 63.10 to 108.44 m² g⁻¹ and 0.04 to 0.07 cm³ g⁻¹, respectively, due to the partial decomposition of the PVP and the formation of the porous structure. The average pore diameter for these samples was 4.50 and 3.96 nm, respectively. High specific surface areas increase the number of active sites, improving adsorption/photocatalytic performance³³. For samples calcined at higher temperatures, the surface area decreases with increasing temperature from 450 to 550 °C, which was from 53.49 to 24.78 m² g⁻¹. In these temperatures,

the sample calcined at 500 °C exhibited the highest average pore diameter of 15.30 nm and those calcined at 450 and 550 °C were 9.95 and 12.8 nm, respectively. This suggested that the relatively higher average pore size decreased the surface area of those samples. The results demonstrate that PVP can be successfully used not only as a source of carbon and nitrogen but also as a pore-forming agent in ceramic nanofibers⁴⁴. The pore characteristics were dependent on the calcination temperature.

Figures 6a and 6b depict the Tauc plot by the Kubelka-Munk method analyzed with the diffuse reflectance data of all samples. The results show that the content of carbon influenced the band energy of the fibers obtained. All samples presented gap energies lower than those of pure TiO₂ (3.2 eV)^{7,9}.

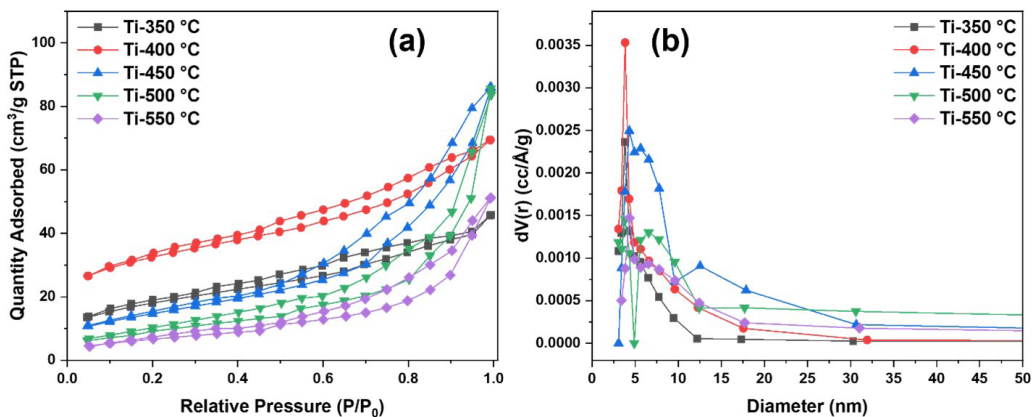


Figure 5. (a) N₂ adsorption-desorption isothermal curves, and (b) pore diameter distribution of nanofibers prepared at different temperatures.

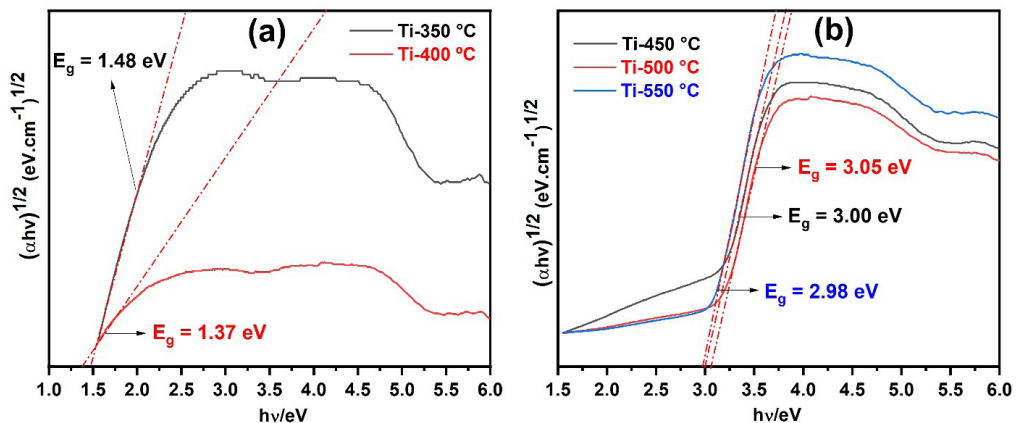


Figure 6. Tauc plots of Ti nanofibers prepared at different temperatures.

Table 1. Physical parameters of Ti nanofibers at different temperatures.

	BET [m ² g ⁻¹]	BJH pore volume [cm ³ g ⁻¹]	BJH average Pore Diameter [nm]	BJH Pore area [m ² g ⁻¹]
Ti-350 °C	63.10	0.04	4.50	26.35
Ti-400 °C	108.44	0.07	3.96	38.70
Ti-450 °C	53.49	0.13	9.95	54.62
Ti-500 °C	34.60	0.13	15.30	38.44
Ti-550 °C	24.78	0.08	12.80	28.58

The lowest band gap values were for the samples calcined at 350 and 400 °C with energy gaps of 1.48 and 1.37 eV, respectively (Figure 6a). However, these results may also have been affected by the disordered and non-crystalline nature of these samples since the Ti-350 °C is amorphous and the Ti-400 °C has only 50% crystallinity (see Figure 4b). For samples calcined at higher temperatures (450, 500, and 550 °C), the gap energies were closer to those reported for pure TiO₂ (Figure 6b). However, it is also notable that the values were influenced by the amount of carbon in contact with the TiO₂, corroborating the elemental analysis data. For these samples, the greater the amount of carbon,

the smaller the band gap. Thus, the band gap values were 3.00, 3.05, and 2.98 eV for Ti-450 °C, Ti-500 °C, and Ti-550 °C nanofibers, respectively. In addition, the lowest value of Ti-550 °C nanofiber can also be influenced by its higher crystallinity ($X_c = 88\%$). Martins et al.²⁵ prepared N-doped carbon quantum dots/TiO₂ composite by a hydrothermal method with similar band gap value to improve its photocatalytic activity under visible light irradiation.

Figure 7 shows the comparison of the adsorption test (dark condition) (Figure 7a) and the photocatalytic tests using both UV light (Figure 7b) and visible light (Figure 7c).

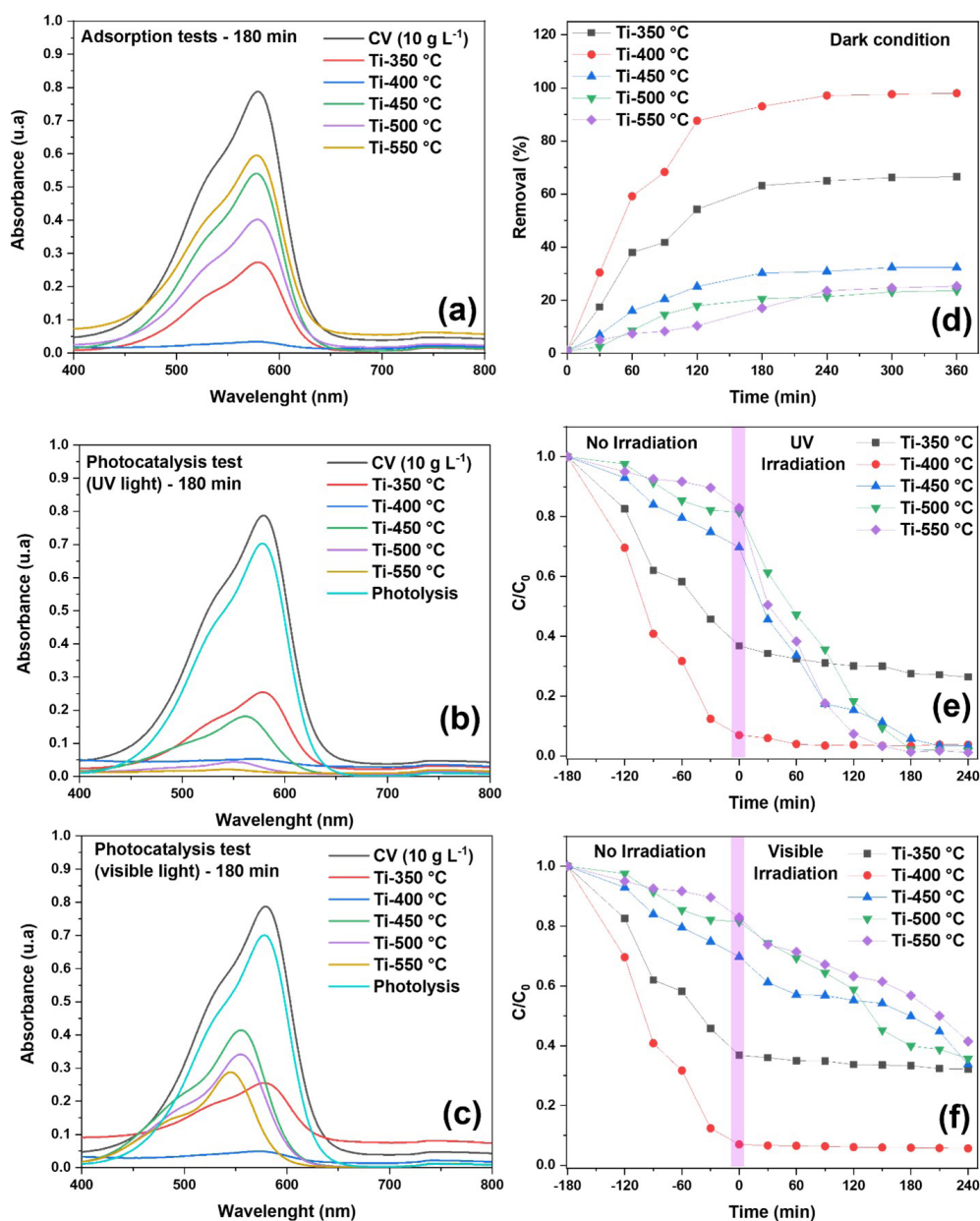


Figure 7. Adsorption test (a), photocatalysis test under UV light (b), and visible light (c), removal percentage in dark condition (0 to 360 min, adsorption) (d), adsorption (-180 to 0 min)/degradation (0 to 240 min) of the CV using the Ti nanofibers prepared at different temperatures: under UV light conditions (e) and Visible light conditions (f). All tests were carried out at pH 7.

The curves were obtained after 180 min of reaction without no equilibrium adsorption/desorption time. The photolysis test showed no significant degradation effect in any of the lights. Comparing the curves of the adsorption tests, it is possible to note that the samples calcined at 350 and 400 °C showed greater dye removal. This can be due to their higher surface area and the higher amount of carbon in these samples associated with the nitrogen content, leaving the surface negatively charged. It means that the cationic dye can electrostatically interact with the negative surface charge of the samples. Figure 7d shows that adsorption/desorption equilibrium occurs in approximately 180 minutes for all samples. Furthermore, it is also observed that these samples did not show sensitivity to light, since no change in dye removal values was observed when the UV light (Figure 7e) and Visible light (Figure 7f) were turned on. This may be related to the lack of order in the structure of these samples or because the interaction between photons and samples is inhibited by the active sites completely covered with dye molecules⁶².

On the other hand, samples calcined at higher temperatures showed both adsorptive and degradation characteristics. For these samples, it is notable to observe the degradation of the dye, since there was a hypsochromic shift in the maximum absorbance to shorter wavelengths (from 580 to 555 nm) due to their interaction with light energy. This could be due to photochemical reactions caused in the chromophore groups of the CV, leading to the breaking of chemical bonds and changes in the electronic structure, similar results were obtained by Zhang et al.⁶⁵. There was a change in the color of the CV to light pink and, consequently, its spectral properties. Although these samples have a smaller surface area than the Ti-350 °C and Ti-400 °C samples, the photocatalytic activity may be enhanced due to the easy penetration of the dye molecules by the higher pores.

Figure 8 shows the percentage of dye removal in the absence of light (before turning on the light) and the percentage of degradation after turning on the light. For samples calcined at 350 °C and 400 °C, the removal efficiency was 67% and 98% in dark conditions, respectively. On the other hand, Ti-450 °C, Ti-500 °C, and Ti-550 °C nanofibers degraded approximately 3-fold more dye from the solution in the presence of UV light than in the dark. The highest degradation efficiency was achieved for the Ti-550 °C sample, 98% when using using UV light. For this sample, approximately 2.5-fold more dye was removed from the solution in the presence of visible light than in the dark. This result is consistent with the lower band gap value attributed to this sample (Ti-550 °C), probably due to the better interaction of carbon in contact with TiO₂ leading to greater

electron photoexcitation and enhancing the photocatalytic activity⁶⁶. Furthermore, Martins et al.²⁵ observed that the occurrence of the Ti-O-C bond in TiO₂/carbon promotes charge transfer and effectively extends light absorption to longer wavelengths. It may justify the reactions that occur under visible light, which reached approximately 50% dye degradation for these samples.

Table 2 shows the kinetic data of the samples that showed good photodegradation efficiency (i.e., Ti-450 °C, Ti-500 °C, and Ti-550 °C). According to Equation 2, the results followed the pseudo-first-order kinetic model, which can be confirmed by the correlation coefficient (R²) for those samples^{53,67}. The rate constant (K) for CV photodegradation estimated was greater for the reaction under UV light than visible light for all samples analyzed. Ti-450 °C, Ti-500 °C, and Ti-550 °C showed good efficiency of 95%, 97%, and 98% (under UV light) within 240 min with a photodegradation rate constant (K) of 0.0133 min⁻¹, 0.01833 min⁻¹ and 0.01974 min⁻¹, respectively. At the same time and under visible light, the efficiency of those samples was 52%, 56%, and 50% with a photodegradation rate constant (K) of 0.00232 min⁻¹, 0.00373 min⁻¹ and 0.00249 min⁻¹, respectively. These results may be due to the band gap energies of the samples, where their values followed the order Ti-500 °C > Ti-450 °C > Ti-550 °C. The same order is attributed to the amount of carbon in the TiO₂ structure. As is known, pure TiO₂ does not absorb in the visible region³¹, however, in this work, it is suggested that the interaction between carbon and TiO₂ reduced the band gap of the samples, making them photosensitive to visible light.

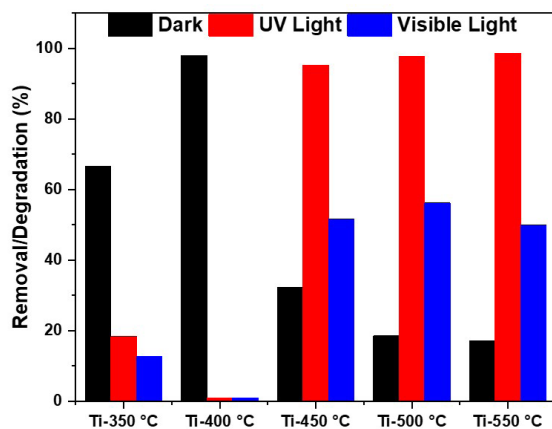


Figure 8. Adsorption percentage (-180 to 0 min) and degradation percentage (0 to 240 min) under UV and Visible light conditions.

Table 2. Kinetic data of Ti nanofibers using crystal violet (CV) 10mgL⁻¹.

	UV light		Visible light	
	K [min ⁻¹]	R ²	K [min ⁻¹]	R ²
Ti-450 °C	0.01333	0.981	0.00232	0.815
Ti-500 °C	0.01833	0.931	0.00373	0.963
Ti-550 °C	0.01974	0.951	0.00249	0.934

4. Conclusion

In summary, TiO₂/C and TiO₂/C/N nanofibers were successfully designed via a facile solution blow spinning method using non-toxic polymer and solvent under controlled synthesis and heat treatment conditions. The findings verified the effectiveness of employing PVP as a source of carbon and nitrogen since the results confirmed the coexistence of C and N. Their content in the TiO₂ structure decreased as the temperature increased from 350 to 550 °C, making it practically insignificant. The physicochemical, morphological, and structural properties were also temperature-dependent. Concerning the diameters and formation of nanofibers, they were practically unaffected by the process parameters, as well as by the calcination temperatures. The results provided evidence that adsorption and photodegradation reactivity were highly correlated with the characteristics of the fibers and the content of associated carbon and nitrogen atoms. Samples calcined at lower temperatures (350 and 400 °C) showed adsorptive properties, while samples calcined at higher temperatures (450-550 °C) showed adsorptive and photocatalytic properties, with photocatalysis predominating. The highest CV removal by adsorption was 98% for Ti-400 °C nanofibers within 360 min and the highest removal by photocatalysis was 98% for Ti-400 °C nanofibers within 240 min under UV light. This good affinity with cationic dyes and dye degradation efficiency in both visible and UV light encourages more detailed future work to better understand the potential of these samples in water treatment.

5. Acknowledgments

This work was supported by the Coordenação de Aperfeiçoamento de Pessoal de Nível Superior – Brasil (CAPES), by postdoctoral fellowship (PNPD/CAPES), grant no 88887.464025/2019-00, and by the Conselho Nacional de Desenvolvimento Científico e Tecnológico – CNPq, grant nos. 420004/2018-1 and 309771/2021-8.

6. References

1. Obaideen K, Shehata N, Sayed ET, Abdalkareem MA, Mahmoud MS, Olabi AG. The role of wastewater treatment in achieving sustainable development goals (SDGs) and sustainability guidelines. *Energy Nexus*. 2022;7:100112.
2. Battiston S, Rigo C, Severo EC, Mazutti MA, Kuhn RC, Gündel A, et al. Synthesis of zinc aluminate (ZnAl₂O₄) spinel and its application as photocatalyst. *Mater Res*. 2014;17(3):734-8.
3. Silvestri S, Stefanello N, Salla JS, Foletto EL. Photocatalytic properties of Zn₂SnO₄ powders prepared by different modified hydrothermal routes. *Res Chem Intermed*. 2019;45:4299-313.
4. Silvestri S, Trentin RS, Salla JS, Foletto EL. Improved photocatalytic performance for rhodamine B degradation by porous Zn₂SnO₄ prepared with carbon black as a pore-forming agent. *Water Air Soil Pollut*. 2019;230:186.
5. Haleem A, Shafiq A, Chen SQ, Nazar M. A comprehensive review on adsorption, photocatalytic and chemical degradation of dyes and nitro-compounds over different kinds of porous and composite materials. *Molecules*. 2023;28:1081.
6. Hasanpour M, Hatami M. Photocatalytic performance of aerogels for organic dyes removal from wastewaters: review study. *J Mol Liq*. 2020;309:113094.
7. Moridon SNF, Arifin K, Yunus RM, Minggu LJ, Kassim MB. Photocatalytic water splitting performance of TiO₂ sensitized by metal chalcogenides: A review. *Ceram Int*. 2022;48(5):5892-907.
8. Etacheri V, Valentin CD, Schneider J, Bahnemann D, Pillali SC. Visible-light activation of TiO₂ photocatalysts: advances in theory and experiments. *J Photochem Photobiol Photochem Rev*. 2015;25:1-29.
9. Akhter P, Arshad A, Saleem A, Hussain M. Recent development in non-metal-doped titanium dioxide photocatalysts for different dyes degradation and the study of their strategic factors: a review. *Catalysts*. 2022;12:1331.
10. Xie S, Su H, Wei W, Li M, Tong Y, Mao Z. Remarkable photoelectrochemical performance of carbon dots sensitized tio₂ under visible light irradiation. *J Mater Chem A Mater Energy Sustain*. 2014;2(39):16365-8.
11. Al-Madanat O, Alsalka Y, Ramadan W, Bahnemann DW. TiO₂ photocatalysis for the transformation of aromatic water pollutants into fuels. *Catalysts*. 2021;11(3):317.
12. Lu D, Qin L, Liu D, Sun P, Liu F, Lu G. High-efficiency dye-sensitized solar cells based on bilayer structured photoanode consisting of carbon nanofiber/TiO₂ composites and Ag@TiO₂ core-shell spheres. *Electrochim Acta*. 2018;292:180-9.
13. Li Y, Li R, Jin Y, Zhao W, Chen J, Chen G, et al. A novel TiO₂ nanoparticle-decorated helical carbon nanofiber composite as an anode material for sodium-ion batteries. *J Electroanal Chem (Lausanne)*. 2021;901:115765.
14. Liang Y, Li N, Li F, Xu Z. Controllable nitrogen doping and specific surface from freestanding TiO₂@carbon nanofibers as anodes for lithium ion battery. *Electrochim Acta*. 2019;297:1063-70.
15. Yao M, Li L, Yao T, Wang D, Liu B, Wang H. Embedding anatase TiO₂ nanoparticles into holey carbon nanofibers for high-performance sodium/lithium ion batteries. *J Alloys Compd*. 2022;926:166943.
16. Tang K, Li Y, Cao H, Su C, Zhang Z, Zhang Y. Amorphous-crystalline TiO₂/carbon nanofibers composite electrode by one-step electrospinning for symmetric supercapacitor. *Electrochim Acta*. 2016;190:678-88.
17. Kolathodi MS, Natarajan TS. Development of high-performance flexible solid state supercapacitor based on activated carbon and electrospun TiO₂ nanofibers. *Scr Mater*. 2015;101:84-6.
18. Arkan E, Paimard G, Moradi K. A novel electrochemical sensor based on electrospun TiO₂ nanoparticles/carbon nanofibers for determination of Idarubicin in biological samples. *J Electroanal Chem*. 2017;801:480-7.
19. Saud PS, Pant B, Alam A-M, Ghouri ZK, Park M, Kim HY, et al. Carbon quantum dots anchored TiO₂ nanofibers: effective photocatalyst for wastewater treatment. *Ceram Int*. 2015;9:11953-9.
20. Li Y, Wang Z, Zhao H, Yang M. Composite of TiO₂ nanoparticles and carbon nanotubes loaded on poly(methyl methacrylate) nanofibers: preparation and photocatalytic performance. *Synth Met*. 2020;269:116529.
21. Kumar PS, Venkatesh K, Gui EL, Jayaraman S. Electrospun carbon nanofibers/TiO₂-PAN hybrid membranes for effective removal of metal ions and cationic dye. *Environ Nanotechnol Monit Manag*. 2018;10:366-76.
22. Liang Y, Zhou B, Li N, Liu L. Enhanced dye photocatalysis and recycling abilities of semi-wrapped TiO₂@carbon nanofibers formed via foaming agent driving. *Ceram Int*. 2018;44(2):1711-8.
23. Jiang L, Huang Y, Liu T. Enhanced visible-light photocatalytic performance of electrospun carbon-doped TiO₂/halloysite nanotube hybrid nanofibers. *J Colloid Interface Sci*. 2015;439:62-8.
24. Qiu J, Liu F, Yue C, Ling C, Li A. A recyclable nanosheet of Mo/N-doped TiO₂ nanorods decorated on carbon nanofibers for organic pollutants degradation under simulated sunlight irradiation. *Chemosphere*. 2019;215:280-93.
25. Martins NCT, Ângelo J, Girão AV, Trindade T, Andrade L, Mendes A. N-doped carbon quantum dots/TiO₂ composite with improved photocatalytic activity. *Appl Catal B*. 2016;193:67-74.
26. Silvestri S, Stefanello N, Sulkovski AA, Foletto EL. Preparation of TiO₂ supported on MDF biochar for simultaneous removal of methylene blue by adsorption and photocatalysis. *J Chem Technol Biotechnol*. 2019;95(10):2723-9.

27. Cheng C, Lu D, Shen B, Liu YD, Lei J, Wang L, et al. Mesoporous silica-based carbon dot/TiO₂ photocatalyst for efficient organic pollutant degradation. *Microporous Mesoporous Mater.* 2016;226:79-87.
28. Varnagiris S, Medvids A, Lelis M, Milcius D, Antuzevics A. Black carbon-doped TiO₂ films: synthesis, characterization and photocatalysis. *J Photochem Photobiol Chem.* 2019;382:111941.
29. Dong C, Xing M, Lei J, Zhang J. TiO₂/carbon composite nanomaterials for photocatalysis. In: Wang X, Anpo M, Fu X, editors. *Current developments in photocatalysis and photocatalytic materials.* USA: Elsevier; 2020. p. 303-21.
30. Wang C, Yu R. Highly efficient visible light photocatalysis of tablet-like carbon-doped TiO₂ photocatalysts via pyrolysis of cellulose/MIL-125 (Ti) at low temperature. *J Solid State Chem.* 2022;309:122992.
31. Jarvin M, Rosaline DR, Gopalakrishnan T, Kamalam MBR, Foletto EL, Dotto GL, et al. Remarkable photocatalytic performances towards pollutant degradation under sunlight and enhanced electrochemical properties of TiO₂/polymer nanohybrids. *Environ Sci Pollut Res Int.* 2023;30(22):62832-46.
32. Jarvin M, Kumar SA, Rosaline DR, Foletto EL, Dotto GL, Inbanathan SSR. Remarkable sunlight-driven photocatalytic performance of Ag-doped ZnO nanoparticles prepared by green synthesis for degradation of emerging pollutants in water. *Environ Sci Pollut Res Int.* 2022;29:57330-44.
33. Zhang J, Fu J, Chen S, Lv J, Dai K. 1D carbon nanofibers@TiO₂ core-shell nanocomposites with enhanced photocatalytic activity toward CO₂ reduction. *J Alloys Compd.* 2018;746:168-76.
34. Sabzehmeidani MM, Mahnaee S, Ghaedi M, Heidari H, Roy VAL. Carbon based materials: a review of adsorbents for inorganic and organic compounds. *Adv Mater.* 2021;2:598-627.
35. Brombilla VL, Lazarotto JS, Silvestri S, Anschau KF, Dotto GL, Foletto EL. Biochar derived from yerba-mate (*Ilex paraguariensis*) as an alternative TiO₂ support for enhancement of photocatalytic activity toward Rhodamine-B degradation in water. *Chem Eng Commun.* 2022;209(10):1334-47.
36. Soffian MS, Halim FZA, Aziz F, Rahman MA. Carbon-based material derived from biomass waste for wastewater treatment. *Environ. Adv.* 2022;9:100259.
37. Farias RMC, Mota MF, Severo LL, Medeiros ES, Klamczynski AP, Avena-Bustillos RJ, et al. Green synthesis of porous N-Carbon/Silica nanofibers by solution blow spinning and evaluation of their efficiency in dye adsorption. *J Mater Res Technol.* 2020;9(3):3038-46.
38. Pant B, Ojha GP, Acharya J, Park M. Ag₃PO₄-TiO₂-carbon nanofiber composite: an efficient visible-light photocatalyst obtained from electrospinning and hydrothermal methods. *Separ Purif Tech.* 2021;276:119400.
39. Pant B, Pant HR, Barakat NAM, Park M. Carbon nanofibers decorated with binary semiconductor (TiO₂/ZnO) nanocomposites for the effective removal of organic pollutants and the enhancement of antibacterial activities. *Ceram Int.* 2013;19:7029-35.
40. Yousef A, Brooks R, Elhalwany M, El-Newehy MH. CuO/S-doped TiO₂ nanoparticles-decorated carbon nanofibers as novel and efficient photocatalyst for hydrogen generation from ammonia borane. *Ceram Int.* 2015;42:1507-12.
41. Xue J, Wu T, Dai Y, Xia Y. Electrospinning and electrospun nanofibers: methods, materials, and applications. *Chem Rev.* 2019;119(8):5298-415.
42. Nadaf A, Gupta A, Hasan N, Fauziya, Kesharwani P, Ahmad S et al. Recent update on electrospinning and electrospun nanofibers: current trends and their applications. *RSC Adv.* 2022;12:23808-28.
43. Medeiros ES, Glenn GM, Klamczynski AP, Orts WJ, Mattoso LHC. Solution blow spinning: a new method to produce micro- and nanofibers from polymer solutions. *J Appl Polym Sci.* 2009;113:2322-30.
44. Dadol GC, Kilic A, Tijing LD, Lim KJA, Cabatangan L, Tan NPB, et al. Solution blow spinning (SBS) and SBS-spun nanofibers: materials, methods, and applications. *Mater Today Commun.* 2020;25:101656.
45. Farias RMC, Severo LL, Costa DL, Medeiros ES, Glenn GM, Santana LNL, et al. Solution blow spun spinel ferrite and highly porous silica nanofibers. *Ceram Int.* 2018;44:10984-9.
46. Silva VD, Medeiros ES, Macedo DA, Simões TA. Engineering of Nb₂O₅ sub-micrometric fibers from metal oxide precursor nanoparticles by Solution Blow Spinning. *Ceram Int.* 2023;49(10):15649-54.
47. Ardestani SS, Bonan RF, Mota MF, Farias RMC, Menezes RR, Bonan PRF, et al. Effect of the incorporation of silica blow spun nanofibers containing silver nanoparticles (SiO₂/Ag) on the mechanical, physicochemical, and biological properties of a low-viscosity bulk-fill composite resin. *Dent Mater.* 2021;37(10):1615-29.
48. Silva VC, Farias RMC, Bonan RF, Cartaxo JM, Medeiros ES, Figueiredo LRF, et al. Novel synthesis of BCP cotton-wool-like nanofibrous scaffolds by air-heated solution blow spinning (A-HSBS) technique. *Ceram Int.* 2023;49(14):24084-92.
49. Qiu L-P, Zhang Y-R, Gao S-L, Zheng Q, Zhang T, Cheng G, et al. Fabrication and magnetic properties of SiO₂ nanoparticles-doped BSCCO superconducting nanofibers by solution blow spinning. *Physica C.* 2023;608:1354251.
50. Farias RMDC, Menezes RR, Oliveira JE, Medeiros ES. Production of submicrometric fibers of mullite by solution blow spinning (SBS). *Mater Lett.* 2015;149:47-9.
51. Costa DL, Leite RS, Neves GA, Santana L, Medeiros ES, Menezes RR. Synthesis of TiO₂ and ZnO nano and submicrometric fibers by solution blow spinning. *Mater Lett.* 2016;183:109-13.
52. Santos AM, Mota MF, Leite RS, Neves GA, Medeiros ES, Menezes RR. Solution blow spun titania nanofibers from solutions of high inorganic/organic precursor ratio. *Ceram Int.* 2018;44:1681-9.
53. Araujo RN, Nascimento EP, Firmino HCT, Macedo DA, Neves GA, Morales MA, et al. α-Fe₂O₃ fibers: an efficient photocatalyst for dye degradation under visible light. *J Alloys Compd.* 2021;882:160683.
54. Nascimento EP, Firmino HCT, Santos AMC, Sales HB, Silva VD, Macedo DA, et al. Facile synthesis of hollow F-doped SnO₂ nanofibers and their efficiency in ethanol sensing. *J Am Ceram.* 2021;104(3):1297-308.
55. Nasouri K, Shoushtari AM, Mojtahedi MRM. Thermodynamic studies on polyvinylpyrrolidone solution systems used for fabrication of electrospun nanostructures: effects of the solvent. *Adv Polym Technol.* 2015;34(3):21495.
56. Cena CR, Silva MJ, Malmonge LF, Malmonge JA. Poly(vinylpyrrolidone)sub-microfibers produced by solution blow spinning. *J Polym Res.* 2018;25:238.
57. Raimundo RA, Silva VD, Silva TR, Medeiros ES, Macedo DA, et al. Synthesis and characterization of NiFe-carbon fibers by solution blow spinning and application for the oxygen evolution reaction. *J Phys Chem Solids.* 2022;160:110311.
58. Someswararao MV, Dubey RS, Subbarao PSV, Singh S. Electrospinning process parameters dependent investigation of TiO₂ nanofibers. *Results Phys.* 2018;11:223-31.
59. Chun H-H, Jo W-K. Polymer material-supported titania nanofibers with different polyvinylpyrrolidone to TiO₂ ratios for degradation of vaporous trichloroethylene. *J Ind Eng Chem.* 2014;20(3):1010-5.
60. Surovčík J, Medvecká V, Greguš J, Gregor MT, Anušová A, et al. Characterization of TiO₂ nanofibers with enhanced photocatalytic properties prepared by plasma assisted calcination. *Ceram Int.* 2022;48(24):37322-32.
61. Albitar E, Barrera-Andrade JM, Calzada LA, García-Valdés J, Valenzuela MA, Rojas-García E. Enhancing free cyanide photocatalytic oxidation by rGO/TiO₂P25 composites. *Materials (Basel).* 2022;15(15):5284.

62. Giang NTH, Tan NN, Huong LM, Hai ND, Thinh NT, Phuc NT, et al. Photocatalytic degradation of crystal violet on titanium dioxide/graphene aerogel doped sulfur. *J Mol Struct.* 2023;1271:134031.
63. Tsai C-M, Song C-G, Hung Y-C, Jeong Y-G, Oh SH, Jeong JH, et al. Carbon induced phase transformation in electrospun TiO₂/multiwall carbon nanotube nanofibers. *Ceram Int.* 2017;43(4):3761-8.
64. Alothman ZAA. Review: fundamental aspects of silicate mesoporous materials. *Materials (Basel).* 2012;12:2874-902.
65. Zhang Y, Ren J, Wang Q, Wang S, Li S, Li H. Oxidation characteristics and degradation potential of a dye-decolorizing peroxidase from *Bacillus amyloliquefaciens* for crystal violet dye. *Biochem Eng J.* 2021;168:107930.
66. Waghchaure RH, Adole VA, Kushare SS, Shinde RA, Jagdale BS. Visible light prompted and modified ZnO catalyzed rapid and efficient removal of hazardous crystal violet dye from aqueous solution: a systematic experimental study. *Results Chem.* 2023;5:100773.
67. Karagoz S, Kiremitler NB, Sakir M, Salem S, Onses MS, Sahmetlioglu E, et al. Synthesis of Ag and TiO₂ modified polycaprolactone electrospun nanofibers (PCL/TiO₂-Ag NFs) as a multifunctional material for SERS, photocatalysis and antibacterial applications. *Ecotoxicol Environ Saf.* 2020;188:109856.